

High resolution neutron radiography analysis of proton exchange membrane fuel cells

D.S. Hussey, D.L. Jacobson

National Institute of Standards and Technology, 100 Bureau Dr., MS 8461, Gaithersburg, MD 20899-8461
daniel.hussey@nist.gov
+1-301-95-6465

Abstract

Neutron radiography enables direct visualization and quantification of many water transport phenomena in proton exchange membrane fuel cells (PEMFCs). The advantage of the technique is that neutrons have a long penetration length through most common PEMFC materials of construction (with a $1/e$ length of about 11 cm for aluminum), while having a relatively short $1/e$ length for water (of order 3 mm). This sensitivity to water enables precise measurements via neutron radiography of the water content in an operating PEMFC that are primarily limited by systematic measurement uncertainties. Recent advances in the spatial resolution of neutron detector technology enable direct measurement of the through-plane water content. This new data provides gas diffusion layer water profiles that can serve as input or comparison data for a large class of one-dimensional PEMFC models. In this article, the technique of neutron radiography is discussed, with an emphasis on the quantitative image analysis of the through-plane water content.

KEY WORDS: Neutron radiography, Neutron imaging, Proton exchange membrane fuel cell, Through-plane water content

1. Introduction

Proper water management in proton exchange membrane fuel cells (PEMFCs) is critical to PEMFC performance and durability. PEMFC performance is impaired if the membrane has insufficient water for proton conduction or if the open pore space of the gas diffusion layer (GDL) and catalyst layer (CL) or the gas flow channels becomes saturated with liquid water there is a reduction in reactant flow to the active catalyst sites. PEMFC durability is reduced if water is left in the CL during freeze/thaw cycling which can result in CL or GDL separation from the membrane⁽¹⁾, and excess water in contact with the membrane can result in accelerated membrane thinning⁽²⁾.

One challenge to developing water management strategies is visualizing and accurately measuring the relatively small mass of water (10 mg/cm^2) typically present in the PEMFC. This is a challenge since standard PEMFC hardware is metallic and conducting, which limits inspection by standard imaging techniques such as optical, X-ray or magnetic resonance imaging (MRI). Optical techniques have been used to study slug and droplet flow in the gas channels, as well as water escape from the GDL surface^(3,4). X-ray imaging at synchrotron sources have thinned out endplates to examine small regions of interest, over short periods of time, as the beam intensity causes radiation damage to the membrane polymer⁽⁵⁾. MRI requires reducing the amount of electrically conducting

material to overcome the PEMFC self-shielding of the MRI signal. With these specially designed test sections, MRI is able to rapidly measure the through-plane water content with spatial resolution in the through-plane direction of order 10 μm , though on the order of several 100 μm in the in-plane directions⁽⁶⁾.

The only measurement technique that is able to accurately measure and visualize the water content in PEMFCs using standard materials of construction for fuel cells is neutron radiography. This is owing to the nature of the interaction between the neutron and material being dominated by the strong nuclear force, rather than the electromagnetic interaction. In particular, neutrons strongly interact with hydrogen, while only weakly interacting with aluminum and carbon. This sensitivity to hydrogen enables accurate measurement of the water content typical of standard PEMFCs with water volume resolution of about 10^{-7} cm^3 limited by neutron counting statistics from an image acquisition time of 60 s in a 15 μm pixel (see Section 3.2.1). The very first application of neutron radiography⁽²⁸⁾ to PEMFC research was of the through-plane water content in a fuel cell with an artificially thick membrane electrode assembly (3 thermally bonded Nafion 117⁽²⁴⁾ membranes). The image detector had a spatial resolution of about 50 μm , and achieved this spatial resolution by centroiding an intensified emission from a scintillator. The centroiding algorithm had a long dead time, with a maximum event rate of about 200 Hz, and hence each image was acquired over a period of about a day. Many interesting features of the membrane water content were observed, including an expected gradient from anode to cathode, and depressions in the membrane water content at the interfaces between the thermally bonded membranes. These oscillations were attributed to an incomplete rearrangement of the hydrophobic surfaces of the thermally bonded membranes. As this was the first measurement, the water quantification utilized the gravimetric measurements of the water uptake in Nafion to convert neutron intensity to membrane water content. Further investigations of the through-plane water content were not pursued until later due to the event rate limitation and lack of suitable high resolution imaging detectors. Since conventional neutron scintillator based detectors had a spatial resolution of about 250 μm , the focus of further PEMFC neutron radiography research was the in-plane water content, and the differences between water in the channels versus water in the land regions. A comprehensive review of this initial neutron radiography work has been given by Trabold, *et al.*⁽⁷⁾ Neutron detector technology has progressed significantly in the past decade. As of publication of this article, the state-of-the-art neutron imaging detector spatial resolution is of order 20 μm , allowing direct measurement of the through-plane (anode versus cathode) water content in standard GDL. This progress has been achieved through both dramatic event processing speed enabling high count rate, high resolution microchannel plates detectors and in developments to fabricating thinner scintillators. There have been a few recent articles that have focused on this new development, but without a detailed discussion of the measurement performance of contributions to measurement uncertainties⁽⁸⁻¹⁴⁾. This article will discuss the technique neutron radiography with a focus on high spatial resolution (50 μm to 20 μm) measurements of the through-plane water content in PEMFCs.

2. Neutron radiography facility layout and detectors

2.1 Neutron Sources and Radiography Beamlines

Neutron sources fall into one of two categories, reactor or spallation. In a fission reactor, 2 to 3 neutrons are produced from the fission of uranium, and only one neutron per fission must be captured to sustain the chain reaction. The neutrons from the fission reaction have an energy of order 2 MeV, and must be slowed to meV energies in order to be used for neutron scattering beamlines. The slowing occurs via inelastic scattering in a moderator material, such as water or heavy water. The resulting neutrons have an energy spectrum that is described by a Maxwell-Boltzmann distribution, the peak energy and width of which are determined by the temperature of the moderator. Neutron spectra are often referred to by the mean temperature of the moderator material, two relevant designations being thermal and cold⁽¹⁵⁾. Thermal neutrons have a characteristic temperature of about 40 °C to 50 °C, yielding a mean neutron energy of about 25 meV, while cold neutrons are moderated in a cryogenic liquid and have an energy of about 3 meV. In a typical spallation source, a high energy (GeV) proton beam collides with a neutron-rich nucleus target, such as mercury, tungsten or uranium, knocking out or spallating neutrons from the nucleus. The neutrons from the spallation process are high energy (MeV to GeV) and must also be slowed down by scattering with a moderator material. Two advantages of a reactor source are that it is a continuous source of neutrons of all energies with a high average fluence rate. The advantage of a spallation source is that the neutrons are produced in short (<1 μs) bursts with a large peak fluence rate, but have a smaller integrated fluence rate. Scattering techniques that can make use of the pulsed structure, are best suited to a spallation source. However, typical neutron radiography experiments use the entire neutron spectrum, and therefore a continuous, high integrated fluence rate of neutrons is optimal for studying PEMFC. One exception to this generalization is the SINQ spallation source at the Paul Scherrer Institute in Switzerland, which is a continuous spallation neutron source, with both cold and thermal neutron radiography facilities⁽¹⁶⁾.

Neutron radiography beamlines are relatively simple compared to most scattering instruments, see Figure 1 which depicts the NIST neutron imaging facility layout. An aperture is placed some distance from the neutron source. Moderated neutrons diffuse away from the source, through the aperture to form a beam. The aperture forms a “pin-hole” image of the neutron source downstream at the sample and detector position. Typical dimensions are an aperture with diameter, D , 1 cm, aperture to detector distance, L , 3 m to 15 m. In order to minimize beam intensity loss from scattering in air (thermal neutrons have about a 97 % transmission in air) the distance between the aperture and the sample position is evacuated. At some facilities, filter material such as single crystal Bi, is placed between the aperture and neutron source to reduce the intensity of the gamma-rays and un-moderated fast neutrons both for radiation safety and to reduce image background noise. Bi has a similar electron density as lead and is effective as a gamma-ray filter, but for every 5 cm of filter length, scatters about 50 % of the thermal neutron intensity. The Bi filter also modifies the neutron spectrum due to Bragg diffraction, as shown in Figure 2. The two primary figures of merit for a neutron radiography facility are the L/D ratio and the neutron fluence rate (neutrons $\text{cm}^{-2} \text{s}^{-1}$). The neutron fluence rate determines the image acquisition time needed to reach a given signal-to-noise rate, and is discussed in more detail in section 3.1.1. The L/D ratio, along with the sample-to-detector separation, z , determines the geometric blur, λ_g , which is calculated by

$$\lambda_g = z D / (L - z) \approx z D / L. \quad (1)$$

λ_g defines the minimum spatial resolution achievable for a beamline, assuming that the detector is also capable of a similar or smaller resolution. A larger L/D ratio means that an object can be placed further from the detector, and the image will still be sharp. Since the neutron fluence rate scales with the square of both (1/L) and D, increasing L/D comes at the expense of decreasing the neutron fluence rate, and therefore an increase in the image acquisition time. In high resolution PEMFC imaging, the interest is the through-plane water content. Thus using a slit rather than circular aperture reduces the blur along the dimension of interest, while maintaining a reasonable neutron fluence rate for image acquisition. Most imaging facilities have a set of apertures so as to optimize beam conditions for the imaging application. As an example, the current choice of apertures at the NIST neutron imaging facility, along with the corresponding fluence rates is shown in Table 1. The other means to reduce λ_g is to minimize the dimension of the object along the beam path direction, which means reducing the width of the active area. An additional way to minimize λ_g is to design the test section such that gas and electrical connections are made on one side, allowing the other side of the test section to be mounted flush with the face of the detector. Typical PEMFCs for high resolution neutron imaging are about 1 cm in width, and can be placed about 2 cm from the neutron detector and are imaged with an L/D = 6000. This means that λ_g is about 5 μm , or about 5 times smaller than the intrinsic detector spatial resolution.

2.2 Neutron imaging detectors

Since neutrons are neutral particles, they cannot be directly detected. Instead neutron detectors are composite devices. The first detector component is a thin neutron sensitive region, where a neutron is captured. This nuclear reaction results in the emission of energetic charged particles. The second detector component detects the emitted charged particles, either from scintillation light, or amplifying the charge onto a position sensitive electrode. Two figures of merit for a neutron imaging detector are the spatial resolution and the detection efficiency. Typical imaging detectors have a thermal neutron detection efficiency of at least 15 %. The spatial resolution of the detector is described by a point spread function (PSF), which is often approximated by a Gaussian. The common definition of spatial resolution used in neutron radiography is similar to the Rayleigh criterion for observing diffraction peaks, which is the point at which the PSF reaches about 34 % of the maximum value, which for a Gaussian PSF, with standard deviation σ_d

$$\delta_d = \frac{\sigma_d \pi}{\sqrt{2 \ln(10)}}. \quad (2)$$

The spatial resolution can be measured in a number of ways, including the contrast between two absorbing bars as the bar width and separation is varied, or by measuring the width of a sharp edge⁽¹⁷⁾. The effects of the PSF, including λ_g , on measuring the water profile are discussed in more detail in Section 3.1.5.

The most common neutron imaging detector uses a scintillator viewed by a charge-coupled device (CCD) camera. Because the scintillation light is emitted in all directions,

the spatial resolution of a scintillator is approximately the thickness of the scintillator. Since the neutron detection efficiency is an asymptotic function of the thickness, reducing the scintillator thickness in order to increase spatial resolution comes at the cost of counting statistics (water volume resolution). CCDs are sensitive to radiation damage. Thus, CCDs must be located outside of the main beam, typically with a mirror reflection, resulting in reduced light collection. The high resolution imaging system developed at PSI uses a variety of scintillators to optimize the spatial resolution and image acquisition time for a given application. A mirror reflects the light out of the main beam path. A special lens with an f-stop of 1, magnification of 1 to 1 with no vignetting focuses the scintillation light onto a CCD sensor⁽¹⁸⁾. With this system, a variety of scintillators were tested, and with a 10 μm thick gadolinium oxysulfide scintillator a resolution approaching 20 μm was achieved.

Another approach to high resolution neutron imaging is based on microchannel plates (MCP). In these devices, the neutron is captured in the wall of the MCP. The charged particle products from the nuclear reaction after neutron capture exit into the pores of the MCP, knocking out electrons at the wall-pore interface. A negative high voltage (about -5 kV) gives rise to an electron avalanche, which amplifies the initial charge by a factor of order 10^6 . This charge cloud is imaged with a position sensitive anode. The spatial resolution depends on the pore-to-pore separation and the range of the charged particle. Since the charged particles are emitted in all directions, the limit to the spatial resolution is the charge particle range. Current technology has a pore diameter of 10 μm , a pore-to-pore separation of 12 μm , and a charge particle range of about 5 μm , which yields a spatial resolution of about 25 μm ⁽¹⁹⁾. Future detectors are anticipated with a MCP pore diameter of 6 μm , which should result in a detector resolution less than 15 μm ⁽²⁰⁾. Since the MCP system is an event-based detector (as opposed to CCDs which are integrating detectors) the electronic dead-time limits the overall event rate, which for a given neutron fluence rate limits the field of view (FOV). In the case of cross-delay-line anode readout electronics, there is a 10 % dead-time for an overall event rate of about 200 kHz. For an incident fluence rate of about $10^6 \text{ cm}^{-2} \text{ s}^{-1}$, the FOV is limited to about 1 cm^2 . Future readouts using a cross-strip anode are expected to have a factor of ten higher event rate and higher spatial resolution than the cross-delay-line anode⁽²¹⁾.

In high resolution imaging sample mounting and alignment are critical to ensure that the test section is stable and the through-plane direction is well-aligned with the neutron beam axis. (This is the only axis that must be aligned, as other misalignments introduce a relative uncertainty in the measured water thickness that scale as $1/\cos(\theta)$ or about 10^{-4} .) For instance, for a 1 cm wide active area and a pixel pitch of 15 μm requires an angular alignment to about 0.1° , which is easily achieved with standard motorized rotation and tilt stages. The alignment is performed by minimizing the width of the through-direction. The measured width is a parabola as a function of angle, and the minimum of the parabola is the alignment position. With the high spatial resolution, small changes in the test section position can result in poor image registration. Sample position changes can result from thermal expansion, changing a fitting on the cell, or stress in the gas or electrical connections. Incorporating robust mounting into the test section design can reduce many of these issues.

3. Water metrology with neutron radiography

3.1 Neutron attenuation coefficient of water, μ_w

For thermal and cold neutron radiography, the neutron can be treated as a point particle, and the interaction with material can be characterized by a collision cross-sectional area or total neutron scattering cross-section, σ_{tot} , encompassing coherent scattering (i.e. Bragg diffraction), incoherent scattering (resulting from isotopic variation or nuclear spin-flip scattering) and absorption. In a composite material, σ_{tot} is the weighted average over the species present. However, for some composite materials, especially hydrogenous liquids, the cross-section for neutron scattering from hydrogen can depend on the vibrational and rotational excitation modes. These effects can be calculated and properly modeled⁽²²⁾. There is also an energy dependence to the incoherent scattering and absorption processes, with σ_{tot} increasing with decreasing neutron energy. Water exhibits both properties, energy dependent σ_{tot} as shown in Figure 3 and a deviation from the weighted average cross-sections⁽²⁹⁾. The impact of this energy dependence will be discussed below in Section 3.2.2.

Neutron radiography measures the spatially resolved neutron transmission through a sample. The neutron transmission is derived from the Lambert-Beer Law of attenuation, which in differential form is:

$$dI = -IN\sigma_{tot} dt \quad (3)$$

where I is the incident intensity, N is the number density, dt is a differential unit of length. In connection with other transmission methods, the product $N\sigma_{tot}$ is referred to as the attenuation coefficient, μ , with dimension inverse length. For an operating fuel cell, the transmitted intensity is

$$I_w = I_0 \exp(-\mu_{dry} t_{dry} - \mu_w t_w), \quad (4)$$

where, I_0 , is the incident neutron intensity, $\mu_{dry} t_{dry}$ is the attenuation due to the dry components, and $\mu_w t_w$ is the attenuation due to the water in the test section. With a calibration measurement of μ_w , the water thickness, t_w , can be obtained by taking the natural logarithm of the ratio of the operating intensity to the dry intensity. As discussed in Section 2.1, typical active area widths along the neutron beam path are about 1 cm. Assuming a water uptake of 30 % for Nafion, indicates that a minimum thickness for the calibration is about 3 mm. Shown in Figure 4 is the calibration measurement for the BT2 neutron imaging facility, which has a thermal neutron spectrum, shown in Figure 2, and at a temporary imaging location at the end of the cold neutron guide NG1. As one can see from the plot, and Table 2 the cold neutron beam has about a factor of two larger attenuation coefficient than the thermal beam, as expected from the increase in σ_{tot} shown in Figure 3.

The water content in an operating fuel cell is obtained from the ratio of the background (B) corrected images of the operating fuel cell ($I_w = \tilde{I}_w - B$) to the dry fuel cell ($I_d = \tilde{I}_d - B$), where the tilde indicates the raw, measured image:

$$t_w = \frac{-1}{\mu_w} \ln\left(\frac{I_w}{I_d}\right). \quad (5)$$

In order to account for variations in incident neutron intensity, such as reactor power fluctuations or dead-time corrections, one must scale the two images based on the observed intensity in an unchanging region of the image, for instance where there is no sample (open beam) or in the end-plates away from the flow channels. The background in CCD systems is due primarily to the electronic read noise and the dark current. MCP detectors have negligible electronic read noise (which is the advantage of an event-based detector) but have a relative larger sensitivity to gamma-rays from the reactor core that are not completely stopped by the Bi filter. This gamma-ray background can be measured by blocking the thermal neutron beam with a thin plate of borated aluminum (5 mm) and Cd (1 mm), which negligibly reduces the gamma-ray flux from the reactor.

3.2 Sources of Uncertainties in Neutron Radiography

The method of neutron radiography is simple to implement. Since water has a large neutron attenuation coefficient, the technique of radiography has a high sensitivity for small water mass changes, of order 100 ng achievable. There are several contributions to the overall water measurement uncertainty that limit this sensitivity. The primary sources of uncertainty for high resolution imaging of the through-plane water content in PEMFCs are neutron counting statistics, departure from the Lambert-Beer law of attenuation due to beam hardening, uncertainty in the background subtraction of the reactor core and sample prompt gamma-ray radiation, reduction in the measured water content in rapidly changing regions due to image blur, and change in the total neutron scattering from water that is absorbed by Nafion.

3.2.1 Counting Statistics

The water thickness measurement uncertainty due to neutron counting statistics can be calculated from Poisson counting statistics. For a random process, the standard deviation, Δ_I , in the observed counts I , is $\Delta_I = \sqrt{I}$. The number of neutrons in the incident, or open beam, I_0 , is the product of the neutron fluence rate Φ ($\text{cm}^{-2} \text{s}^{-1}$), integration time T (s), integration area A (cm^2) and neutron detection efficiency, η :

$$I_0 = \Phi * \eta * T * A \quad (6)$$

Typical values for through-plane water measurements are $\Phi = 1 \times 10^6 \text{ cm}^{-2} \text{ s}^{-1}$, $T = 100 \text{ s}$, $A = 2.25 \times 10^{-6} \text{ cm}^2$ (pixel area), $\eta = 0.2$, giving a per pixel intensity of $I_0 = 45$, so that $\Delta_I \approx 6.7$, or a 15 % relative uncertainty. Since the dry and background images are static conditions, the counting statistics of the wet image typical determine the the liquid water uncertainty. Taking the partial derivative of Equation (5) with respect to I_w gives the water thickness uncertainty⁽²³⁾ as

$$\Delta_t = \frac{1}{\mu_w} \sqrt{\frac{1}{I_w}} = \frac{1}{\mu_w} \sqrt{\frac{\exp(\mu_w t)}{\phi A T \eta}}. \quad (7)$$

As shown above, $\mu_w = 0.338 \text{ mm}^{-1}$ for the NIST MCP detector system, which means that

for a 100 s exposure, the per pixel one-sigma water thickness uncertainty due to Poisson counting statistics is $\Delta_t \approx 0.45$ mm, or a water volume of about 10^{-7} cm³. In a PEMFC, the minimum sensitivity may be larger than this, as the membrane and the GDLs attenuate the beam. During an experiment, the water thickness sensitivity can be improved by integrating for a longer period of time, integrating the water content along the in-plane direction (for instance, using a “differential cell”), as shown in Figure 5. The sensitivity can also be improved by using a cold neutron beam. Cold neutrons provide two benefits. The first is that the neutron detection efficiency (η) is about a factor of two larger for typical detectors. The second is that the total neutron scattering cross section (Figure 3) increases with decreasing neutron energy, such that the attenuation coefficient (μ) also increases by about a factor of two, as shown in Figure 4. Thus, for equal thermal and cold neutron fluence rates, the standard uncertainty in the measured water thickness for cold neutron radiography is about 35 % smaller than that for thermal neutron radiography.

3.2.2 Beam Hardening

As mentioned above in Section 3.1, the total neutron scattering of water depends on the incident neutron energy. Thus, for sufficiently thick sections of water and high counting statistics data, beam hardening can be observed. Beam hardening results in lower energy neutrons being preferentially scattered or absorbed, and the spectrum of the emerging neutron beam has a higher mean energy. As a result, the object can appear to have a higher transmission and applying equation (5) to a thick region section of water would result in measuring a thinner section of water. In the calibration measurements, this would be manifested by a non-linear relationship between the neutron optical density and water thickness. As shown in Figure 4, the optical density versus water thickness up to 4.5 mm resulted in a linear fit with a reduced χ^2 of about 1, with no evidence for beam hardening beyond the uncertainty due to counting statistics of the measurement. Thus, analyzing typical PEMFC images with equation (5) will introduce a negligible uncertainty compared to that of the counting statistics.

3.2.3 Background Subtraction

A changing background is a source of measurement uncertainty. The background can change from varying CCD temperature, changes in reactor gamma-ray fluence rate that is related to power fluctuations, prompt gamma-rays from the sample, or scattered neutrons. If in equation (5) there is a different background for the wet and dry images that is not properly accounted for, the resulting fractional error in the measured water thickness is

$$\frac{\Delta t_w}{t_w} = -\frac{1}{\mu_w t_w} \ln \left(1 + \frac{(1-P)B}{\exp(-\mu_w t_w) / I_d} \right), \quad (8)$$

where $P = B_w/B$ is the ratio of the wet and dry backgrounds. Shown in Figure 6 is the fractional error for $I_d = 50$, $B = 0.5$. The resulting systematic uncertainty is of the order of or less than the uncertainty due to counting statistics, meaning that varying backgrounds, including that due to scattered neutrons will introduce negligible uncertainty into the measurement of the membrane and GDL water content.

3.2.4 Changes in the total neutron scattering from water absorbed in the membrane

As discussed in Section 3.0, the total neutron scattering cross-section of hydrogenous materials often depend on the rotational and vibrational modes of the molecule. Thus, when water is absorbed in the PEMFC membrane, it is possible that there could be a change in the neutron scattering cross-section. To determine if there is a change in the scattering cross-section, the water sorption of a Nafion 117⁽²⁴⁾ membrane as a function of water activity was measured. A humidified nitrogen gas stream, with a flow of 100 sccm was introduced on either side of a bare membrane at 40 °C and 80 °C. For each relative humidity (RH) condition, the gas was flowed for 30 minutes, and then the 15 minutes of images were acquired, for a total of 45 minutes at each RH condition. (This will result in a lower water sorption value at 100 % RH due to insufficient time to reach equilibrium.) The membrane water content was determined by the value at the center of the membrane. The systematic uncertainty due to the image resolution (as discussed below in Section 3.2.5) was estimated by convolving the PSF due to a 50 μm blur with a model function of a uniform water thickness across the membrane. The simulation was performed for each saturation condition and demonstrated that the relative uncertainty due to spatial resolution was less than 2 %. The water content of the membrane, λ , (reported in moles of water per moles of sulfonic acid) is shown in Figure 7, and there is no evidence for a change in the total neutron scattering cross-section that is larger than the uncertainty due to counting statistics, or of that due to the relative humidity control.

3.2.5 Image Spatial Resolution

The largest source of systematic uncertainty is due to the finite image resolution. The measured image can be described as the convolution of the true sharp image with the imaging system point spread function, PSF. The PSF is reasonably approximated by a Gaussian,

$$PSF(x - x') = \frac{1}{\sqrt{2\pi\sigma_i^2}} \exp\left(-\frac{(x - x')^2}{2\sigma_i^2}\right), \quad (9)$$

where σ_i is related to the overall spatial resolution δ_i by equation (2). There are two independent contributions to δ_i , the geometric blur, λ_g , and the neutron detector spatial resolution, δ_d , so that:

$$\delta_i = \sqrt{\delta_d^2 + \lambda_g^2}. \quad (10)$$

As shown in Figure 8, the spatial resolution effects high resolution PEMFC imaging in two ways. The first effect is that the measured water profile will not contain discontinuous jumps or step-like image features, for instance at the boundary of the catalyst and microporous layer (MPL). Rather, an image of a step change will be described as an error function, with the width determined by δ_i . This is demonstrated in Figure 8 (a), where the transmission through a slab of water is convolved with a PSF described by a $\delta_i = 25 \mu\text{m}$. At the edges of the transition, the neutron transmission significantly deviates from that of the sharp profile. The second effect is a lower observed water content in the water profile in the through-plane direction. The size of the deviation depends both on the thickness of the water and the width. As shown in

Figure 8 (b), as the width of the region approaches $2\delta_i$, the measured neutron transmission at the center of the slab ceases to reach the true transmission value. In through-plane imaging of PEMFCs, the water content is concentrated in the membrane electrode assembly, which is a thin region compared to the image spatial resolution. This is similar to the simulated water profile with a $50\ \mu\text{m}$ width in Figure 8 (a). As shown in Figure 8 (b), significantly less water is observed in the water profile.

This means that if the total water content of the test section is measured from the image,

$$V_{t,I} = -\frac{A_p}{\mu_w} \sum_{j=1}^N \ln\left(\frac{I_{w,j}}{I_{d,j}}\right). \quad (11)$$

the measured water content will be systematically smaller. However, the correct total water content can be obtained from the image. This is because the total water content attenuates the neutron beam as expected, and by calculating the total water content from the average transmission

$$V_{t,a} = -\frac{NA_p}{\mu_w} \left(\ln \sum_j I_{w,j} - \ln \sum_j I_{d,j} \right) \quad (12)$$

will yield an accurate measurement of the water content. In equations (12) and (11), the sum is taken over the entire region of interest of N pixels, and A_p is the area of a single pixel. In other words, the overall transmission of the neutron beam only depends on the amount of water in the test section. This systematic effect is reduced in in-plane PEMFC imaging, as the water thickness that the neutron beam passes through is typically a factor of 10 smaller, and the natural logarithm is nearly linear in transmission.

While the PSF can be modeled, it is not straightforward to deconvolve the images to obtain a sharpened water content. Due to small pixel areas, and weak neutron source, high resolution neutron images are noisy, specifically the signal to noise ratio for high frequency components is very small. Deconvolved images using Wiener filtering show little improvement in the quantitative water content over the unsharpened data, and suffer visually. Other algorithms, such as one based on Maximum Likelihood methods may result in sharper images, with a large computation cost. Instead, rather than attempting to sharpen the measured data, a more robust method of comparison is to simulate the neutron image based on a model prediction of the water content.

4 Recent in situ high resolution neutron radiography experiments of PEMFCs

The improved neutron detector spatial resolution has been a recent advance, with user instruments first available at the end of 2006 and 2007 at NIST and PSI, respectively. The work can be classified as proof-of-principle^(8,9), *in situ* measurement of the steady-state through-plane water content during fuel cell operation⁽¹⁰⁻¹²⁾, and dynamic through-plane mass transport measurements^(13,14).

4.1 Proof-of-principle experiments

The primary results of these first experiments from each facility were primarily proof-of-principle. Hussey, *et al.*⁽⁸⁾ used a MCP detector with intrinsic spatial resolution of 25 μm , and overall image resolution of about 30 μm . With this setup, a test section was operated in a differential cell mode, with a minimum stoichiometric ratio of about 50 on both the anode and cathode. Due to cell motion, it was not possible to quantify the total water content in the cell, but relative changes in the through-plane water content were observed from open circuit voltage, and the water content increased as a function of current density.

Boillat, *et al.*⁽⁹⁾ imaged a 0.15 mm wide slit with three different detector setups. By using a 10 μm Gadox scintillator, tilted at a high angle to the beam direction, a spatial resolution of approaching 20 μm along one direction was reported. Using this system, changes in the through-plane water content in a test section maintained at 70 °C and 1 A cm^{-2} for four different anode and cathode inlet RH conditions were observed. The primary observation was that for under-saturated cathode inlet RH, water collected in the ribs in the cathode GDL.

4.2 *In situ*, steady-state through-plane water content

In the work of Hickner, *et al.*⁽¹⁰⁾, an operating PEMFC, with a Nafion 117 membrane was imaged with 25 μm detector resolution *in situ*, and made a wide range of observations. The center of the test section was about 4 cm from the detector face and the beam L/D was 1200 resulting in an overall spatial resolution of about 50 μm . The through-plane water profile of the cell was measured at different cell temperatures, current densities, and anode and cathode gas feed flow rates, and the counting statistics uncertainty corresponded to a water thickness resolution of about 3 μm for the 800 pixel-wide regions used for the line profiles. Detailed information was obtained on the cross-sectional water content of the gas flow channels and membrane electrode assembly. At low current densities, water was observed to remain on the cathode. Significant water in the anode gas flow channel was observed when the waste heat and water production of the cell were moderate. No significant gradient in water content within the membrane was observed from anode to cathode, which is due to the image spatial resolution. The total liquid water content of the membrane electrode assembly was fairly stable between current densities of 0.25 A cm^{-2} and 1.25 A cm^{-2} even though the water in the gas flow channels changed drastically over this current density range. At 60 °C the water content in the center of the gas diffusion layer was depleted compared to the membrane or gas flow channel interfaces. This phenomenon was not observed at 80 °C where evaporative water removal is prevalent. In a second related article, the measured water content from three operating temperatures at nominally the same current density (0.75 mA cm^{-2}) was compared with calculations from a pseudo two dimensional model⁽¹¹⁾. The quantitative agreement was not very good, due in part to model simplification and not incorporating the instrumental broadening. However, many qualitative trends could be identified, including water transport via the phase change induced flow (heat pipe effect). When the instrumental broadening was incorporated, the model prediction at 80 °C was in reasonable agreement with the measured data.⁽²⁷⁾ However, at lower temperatures, a large discrepancy persists between the measurement and model prediction. This first comparison provided useful insight into required model refinement and image analysis

requirements.

In the work of Spendelow, *et al.*,⁽¹²⁾ high resolution neutron images of water profiles in an operating fuel cell were obtained under varying cell conditions, including temperature, current, inlet humidity, concurrent flow and counter-flow, orientation of the cell to examine effects due to gravity, and the anode flow rate was varied to simulate the effects of a recycle loop. Significantly more water was observed in the MEA during counter-flow operation than under co-flow. This led to a lower high frequency resistance, as well as better cell performance for counter-flow. Rotating the cell vertically such that the anode and cathodes are flipped has a significant effect on the on water density, and it was observed that positioning the anode on top decreases the tendency towards flooding, leading to improved performance.

4.3 Dynamic through-plane mass transport measurements

The focus of Boillat, *et al.*,⁽¹³⁾ was examining the replacement of ^1H (hydrogen) with ^2H (deuterium) in the membrane, which exploits the $\approx 10\times$ smaller neutron cross section for ^2H . The test section was operated with light water and $^1\text{H}_2$ fuel on the anode at two current densities, 0.02 A/cm^2 and 0.80 A/cm^2 . After stabilizing, the fuel (but not the humidifying water) was switched to $^2\text{H}_2$. The authors observed a very rapid increase in the uptake of ^2H , which was faster than that expected solely from the applied current, and further somewhat independent of the current. This rapid exchange indicates a high exchange current density of the hydrogen oxidation reaction. They did not observe a complete replacement of all ^1H in the membrane, only 25 % of the membrane ^1H was exchanged for ^2H , and the authors state that this might be due to the use of light water for humidification.

Kim and Mench⁽¹⁴⁾ used high resolution neutron imaging to visualize the liquid water flow in the through-plane direction under different thermal gradients, and two sets of GDLs, one with only a substrate loading of polytetrafluoroethylene (PTFE) of 5 % by weight and a microporous layer, and with no PTFE content. This visualization work was in support of an extensive series of *ex situ* measurements to determine the water transport rates for thermo-osmosis and phase change induced flow. The GDL with no PTFE showed a slight water flow with no thermal gradient due to the piezometric head. Applying a thermal gradient, so that the liquid side was cooler, prevented the slow leakage water flow. Reversing the thermal gradient resulted in significantly higher fluid flow than in the case of that driven by the piezometric head. Images of the GDL containing PTFE showed that with no thermal gradient, the piezometric head was insufficient to create a flow through the diffusion media. For all cases investigated, when the gas-phase side of the test section was colder, the channels were observed to fill rapidly (few minutes) due to phase change induced flow.

Conclusions

High resolution neutron radiography has enabled the direct measurement of the through-plane water content in PEMFCs. This in turn allows the measurement of a range of water transport properties in the GDL, and in thick membranes. Measurement uncertainties are

dominated by counting statistics and the blurring effects due to the finite spatial resolution. Typical uncertainties due from counting statistics contribute to the membrane water content uncertainties at the 1 % to 5 % level. Depending on the operating conditions, of the PEMFC, primarily at low temperature and high current density, the spatial resolution can result in a large uncertainty. The image spatial resolution can be modeled, and image simulations based on through-plane water content can be easily performed in order to properly account for the instrumental broadening. New detector technology with 10 μm resolution is anticipated to be available in the near future and will further extend the range of investigation. The currently published results have demonstrated the utility of the technique, and it is anticipated that several new reports utilizing the current technology will be published in the near future.

Acknowledgments

This work was supported by the U.S. Department of Commerce, the NIST Ionizing Radiation Division, the Director's office of NIST, the NIST Center for Neutron Research, and the Department of Energy interagency agreement No. DEAI01-01EE50660. The authors wish to acknowledge R. Mukundan, J. Spendelow, R. Borup and J. Davey from Los Alamos National Laboratory for assistance with the water sorption measurements, and E. Baltic at the National Institute of Standards and Technology for technical support.

References

1. He, S.H. and Mench, M.M., "One-dimensional transient model for frost heave in polymer electrolyte fuel cells", *Journal of the Electrochemical Society*, **153**, A1724-A1731 (2006).
2. Huang, X., Wang, X., Preston, J., Bonville, L., Kunz, H. R., Perry, M., and Condit, D., "Effect of Water Management Schemes on the Membrane Durability in PEMFCs", *ECS Transactions*, **16**, 1697, (2008).
3. Spornjak D, Advani SG, Prasad AK, "Simultaneous Neutron and Optical Imaging in PEM Fuel Cells", *Journal of the Electrochemical Society*, **156**, B109-B117 (2009).
4. Wang Y, Wang CY, Chen KS, "Elucidating differences between carbon paper and carbon cloth in polymer electrolyte fuel cells", *Electrochimica Acta*, **52**, 3965-3975, (2007).
5. Hartnig C., Manke I., Kuhn R., Kleinau S., Goebels J., Banhart J, "High-resolution in-plane investigation of the water evolution and transport in PEM fuel cells" *Journal Of Power Sources*, **188**, 468-474 (2009).
6. Tsushima, S., Hirai, S., Kitamura, K., Yamashita, M., Takasel, S., "MRI application for clarifying fuel cell performance with variation of polymer electrolyte membranes: Comparison of water content of a hydrocarbon membrane and a perfluorinated membrane", *Applied Magnetic Resonance*, **32**, 233-241 (2007).
7. T. A. Trabold, J. P. Owejan, J. J. Gagliardo, D. L. Jacobson, D. S. Hussey and M. Arif, "Use of neutron imaging for proton exchange membrane fuel cell (PEMFC) performance analysis and design", *Handbook of Fuel Cells - Fundamentals, Technology and Applications*, Volume 6. Edited by Wolf Vielstich, Harumi Yokokawa, Hubert A. Gasteiger. 2009 John Wiley & Sons, Ltd.
8. D.S. Hussey, D.L. Jacobson, M. Arif, J.P. Owejan, J.J. Gagliardo, T.A. Trabold, "Neutron images of the through-plane water distribution of an operating PEM fuel cell", *Journal of Power Sources*, **172**, 225-228 (2007).
9. Boillat P, Kramer D, Seyfang BC, Frei G, Lehmann E, Scherer GG, Wokaun A, Ichikawa Y, Tasaki Y, Shinohara K, "In situ observation of the water distribution across a PEFC using high resolution neutron radiography", *Electrochemistry Communications*, **10**, 546 (2008).
10. M. A. Hickner, N. P. Siegel, K. S. Chen, D. S. Hussey, D. L. Jacobson, and M. Arif, "In Situ High-Resolution Neutron Radiography of Cross-Sectional Liquid Water Profiles in Proton Exchange Membrane Fuel Cells", *J. Electrochem. Soc.* **155** B427 (2008).
11. A.Z. Weber, M.A. Hickner, "Modeling and high-resolution-imaging studies of water-content profiles in a polymer-electrolyte-fuel-cell membrane-electrode assembly", *Electrochimica Acta*, **53**, 7668-7674 (2008).
12. Jacob Spendelow, R. Mukundan, John Davey, Tommy Rockward, Daniel S. Hussey, David Jacobson, Muhammad Arif, and Rodney L. Borup, "High Resolution Neutron Radiography Imaging of Operating PEM Fuel Cells: Effect of Flow Configuration and Gravity on Water Distribution", *ECS Trans.* **16** (2), 1345 (2008).

13. Boillat P, Scherer GG, Wokaun A, Frei G, Lehmann EH, "Transient observation of H-2 labeled species in an operating PEFC using neutron radiography", *Electrochemistry Communications* 10, **1311** (2008).
14. Soowhan Kim and M. M. Mench, "Investigation of Temperature-Driven Water Transport in Polymer Electrolyte Fuel Cell: Phase-Change-Induced Flow", *J. Electrochem. Soc.* **156** B353 (2009).
15. http://en.wikipedia.org/wiki/Thermal_neutron
16. W.E Fischer, *Physica B* **234** 1202 (1997).
17. Grunzweig C, Frei G, Lehmann E, Kuhne G, David C, "Highly absorbing gadolinium test device to characterize the performance of neutron imaging detector systems", *Review of Scientific Instruments* **78**, 053708 (2007).
18. Lehmann EH, Frei G, Kuhne G, Boillat P, "The micro-setup for neutron imaging: A major step forward to improve the spatial resolution", *Nuclear Instruments & Methods, Section A*, **576**, 389 (2007).
19. Siegmund O.H.W., Vallerger J.V., Martin A., et al., "A high spatial resolution event counting neutron detector using microchannel plates and cross delay line readout", *Nuclear Instruments & Methods, Section A*, **579** 188-191, (2007).
20. Tremsin A.S., Vallerger J.V., McPhate J.B., et al., "On the possibility to image thermal and cold neutron with sub-15 μ m spatial resolution", *Nuclear Instruments & Methods, Section A*, **592**, 374-384 (2008).
21. Siegmund, O.H.W., Tremsin, A.S., Vallerger, J.V., Abiad, R., and Hull, *Nuclear Instruments & Methods, Section A*, **504**, 177 (2003).
22. Edura, Y., Morishima N., "Cold and thermal neutron scattering in liquid water: cross-section model and dynamics of water molecules", *Nuclear Instruments & Methods, Section A*, **534**, 531-543 (2004).
23. Bevington, P.R., *Data reduction and error analysis for the physical sciences*, McGraw-Hill, Boston, 2003, 3rd edition.
24. Certain trade names and company products are mentioned in the text or identified in an illustration in order to adequately specify the experimental procedure and equipment used. In no case does such identification imply recommendation or endorsement by the National Institute of Standards and Technology, nor does it imply that the products are necessarily the best available for the purpose.
25. Springer, T. E., Zawodzinski, T. A., and Gottesfeld, S., "Polymer Electrolyte Fuel Cell Model", *Journal of the Electrochemical Society*, **138**, 2334 (1991).
26. Hinatsu, J.T., Mizuhata, M., and Takenaka, H., "Water Uptake of Perfluorosulfonic Acid Membranes from Liquid Water and Water Vapor", *Journal of the Electrochemical Society*, **141**, 1493, (1994).
27. Hussey, D.S., Jacobson, D.L., Rangachary, M., Borup, R., and Spendelow, J., "Systematic uncertainties in neutron imaging of proton exchange membrane fuel cells", 214th ECS Meeting, Honolulu, HI October 15, (2008).
28. Bellows, R. J. , Lin, M. Y. , Arif, M. , Thompson, A. K., and Jacobson, D., "Neutron Imaging Technique for In Situ Measurement of Water Transport Gradients within Nafion in Polymer Electrolyte Fuel Cells", *Journal of The Electrochemical Society*, **146** 1099-1103 (1999).
29. Melkonian, E., "Slow Neutron Velocity Spectrometer Studies of O₂, N₂A, H₂, H₂O, and Seven Hydrocarbons", *Physical Review*, 76, 1750, (1949), Russell, J.L., Neill, J.M., and Brown, J.R., "Total Cross Section Measurements in H₂O", General Atomic Div. Reports No.7581, 1966, Heinloth, K., "Subthermal Neutron

Scattering on H₂O, CH₂O₂ AND C₆H₆." Zeitschrift fuer Physik, Vol.163,
p.218, 1961.

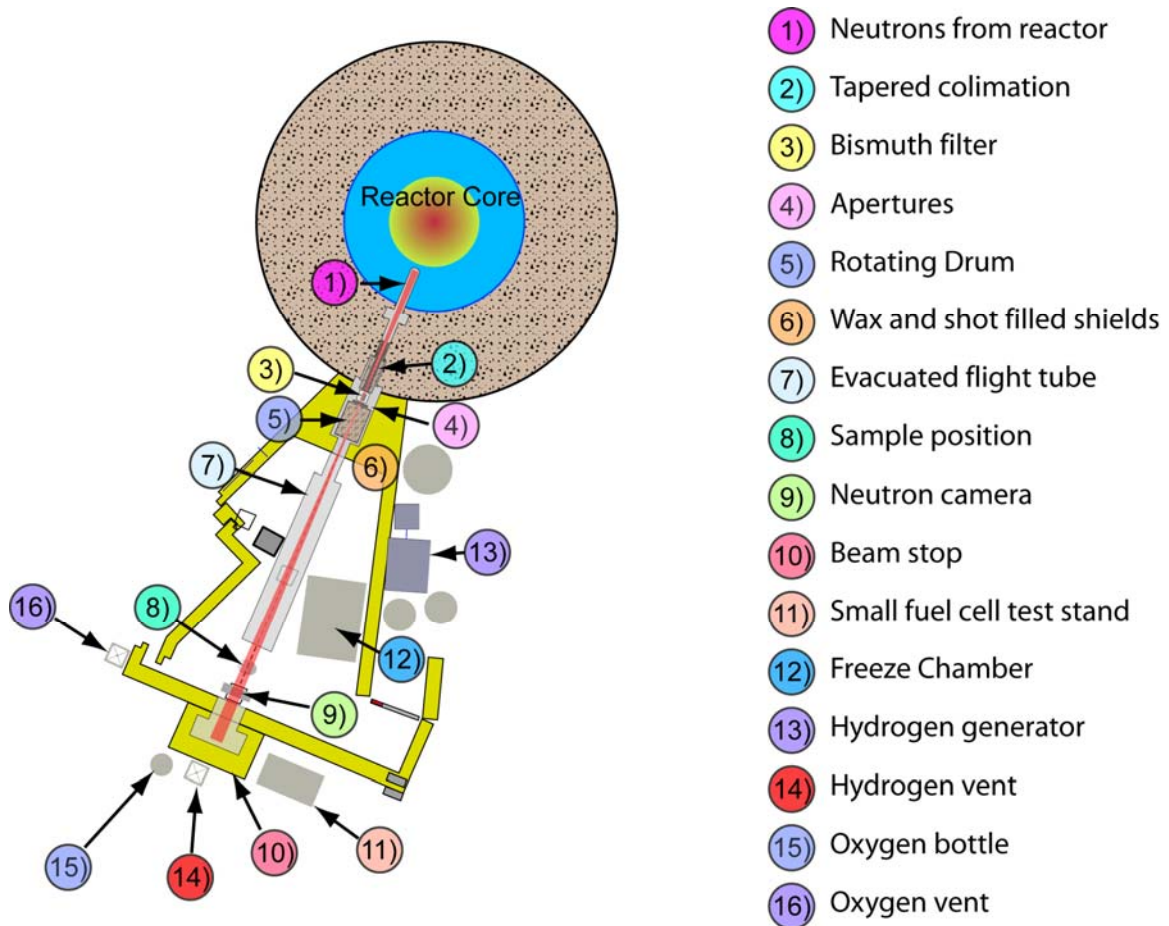


Figure 1: Schematic layout of the NIST BT-2 neutron imaging facility, including the main neutron optic components as well as the location of the fuel cell test and control infrastructure.

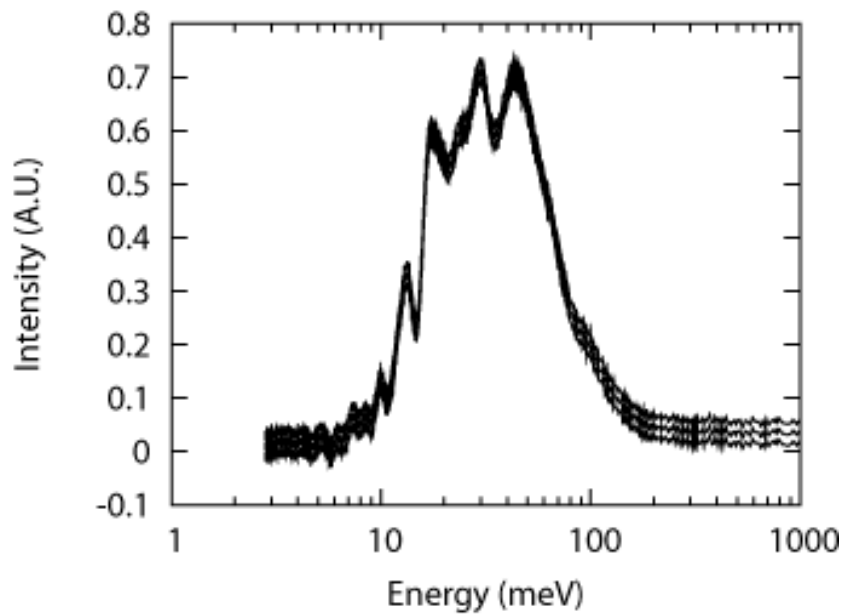


Figure 2: The neutron spectrum at the NIST BT2 neutron imaging facility. The spectrum is not corrected for the neutron detection efficiency, which increases as the square root of the energy.

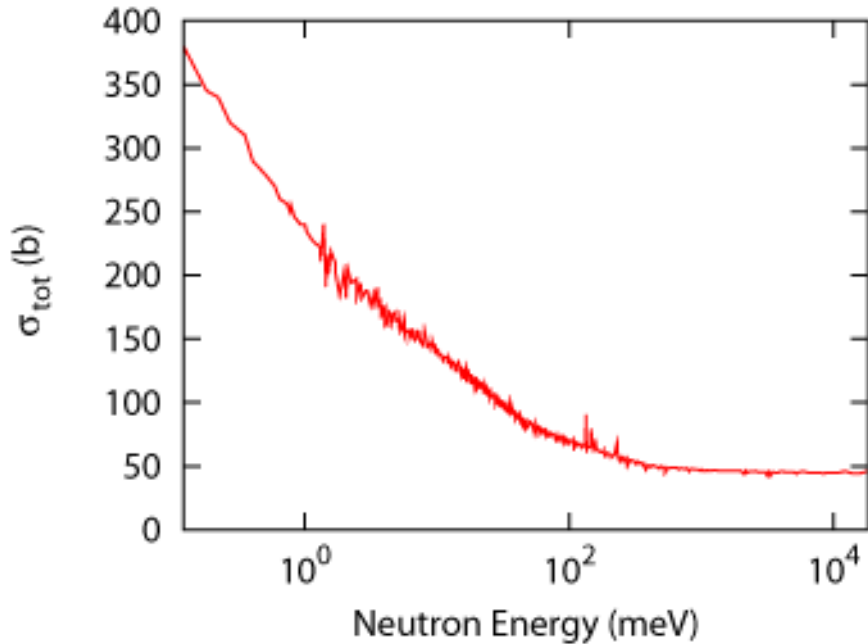


Figure 3: The measured total neutron scattering cross-section for water at 300 K⁽²⁹⁾. The cross-section diverges as the neutron energy approaches 0. Due to this, the transmission through a thick section of water results in the transmitted beam having a modified spectrum, shifted to higher energy. This modification is referred to as beam hardening. Beam hardening is a potential source of systematic uncertainty, as the measured water thickness from applying the Lambert-Beer Law would yield a systematic thinner section of water. In addition, since the measurement resolution is inversely proportional to the σ_{tot} , a neutron beam with a cold neutron energy distribution will have a higher sensitivity than a thermal neutron beam, as shown in Figure 4.

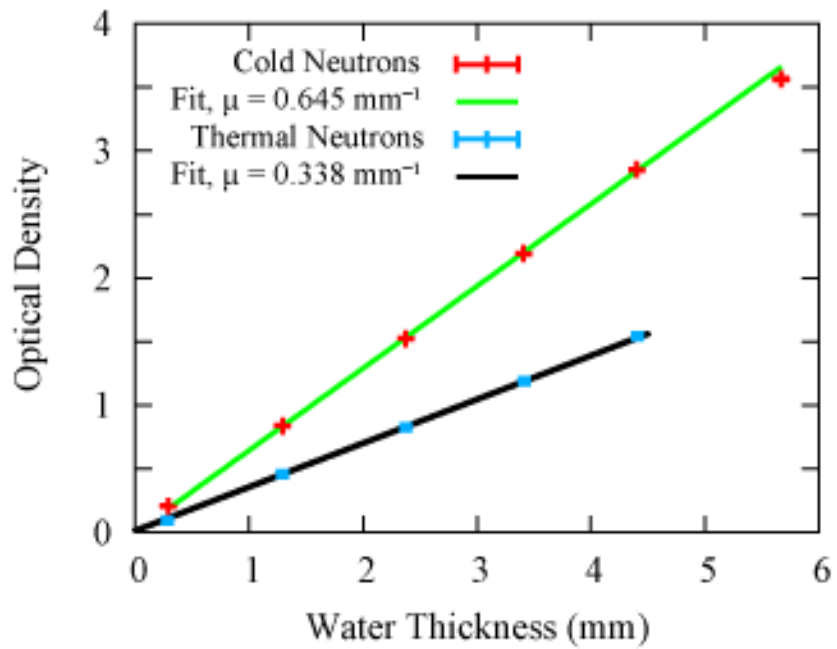


Figure 4: The measured attenuation coefficient for the NIST MCP detector at the BT2 thermal neutron beam and the NG1 cold neutron beam.

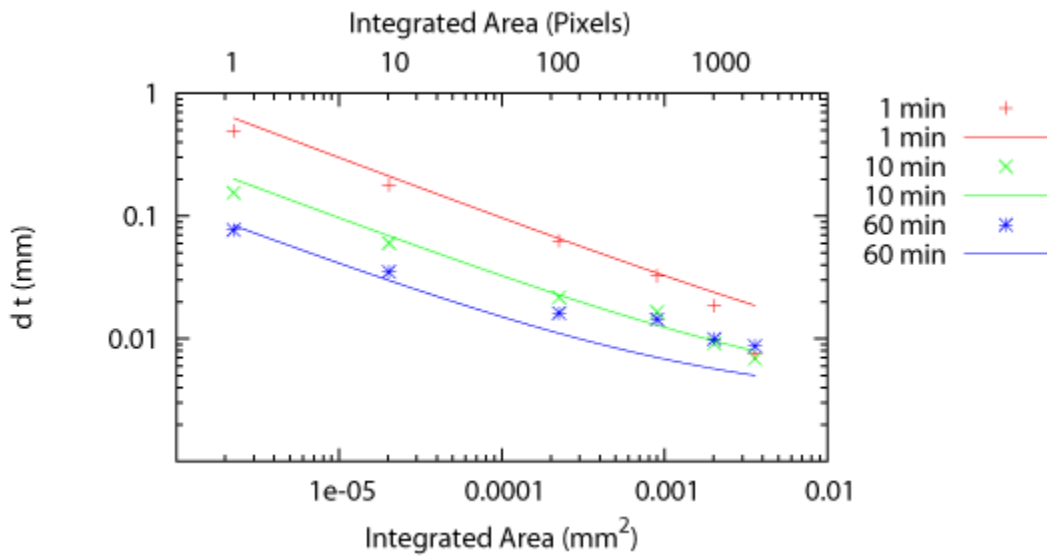


Figure 5: One-sigma measurement uncertainty measured for the MCP detector, a fluence rate of $2 \times 10^6 \text{ cm}^{-2} \text{ s}^{-1}$ as a function of integration area for three different integration times. The solid curves are estimates based on Equation (7). The measured and predicted uncertainties are in reasonable agreement.

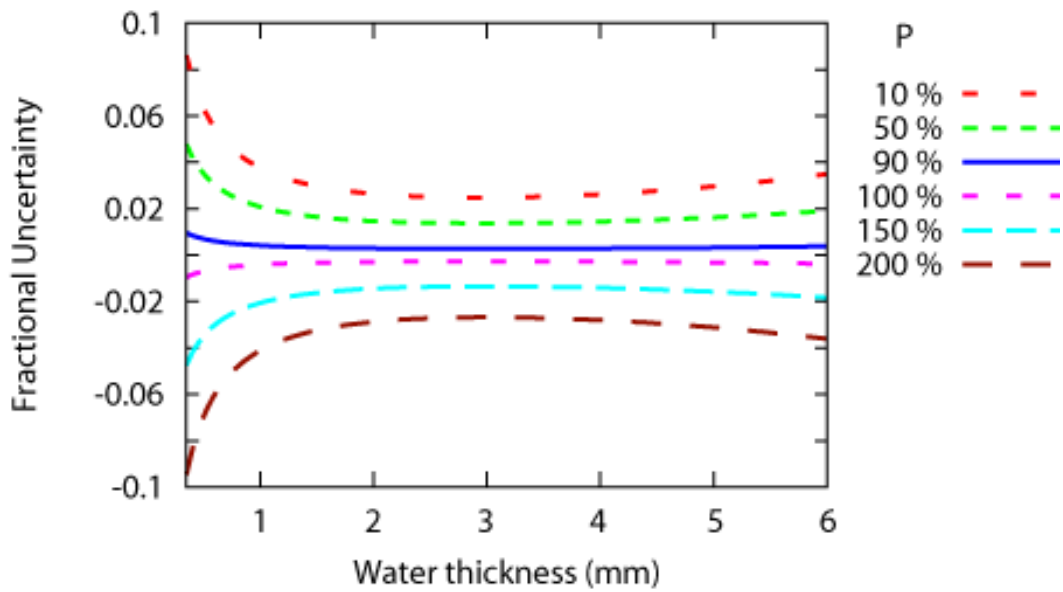


Figure 6: The relative systematic error due to improper background subtraction for an open beam signal to noise ratio of 100. The uncertainty is plotted for the wet image background being a relative percentage of the dry background, $B_w = P B$.

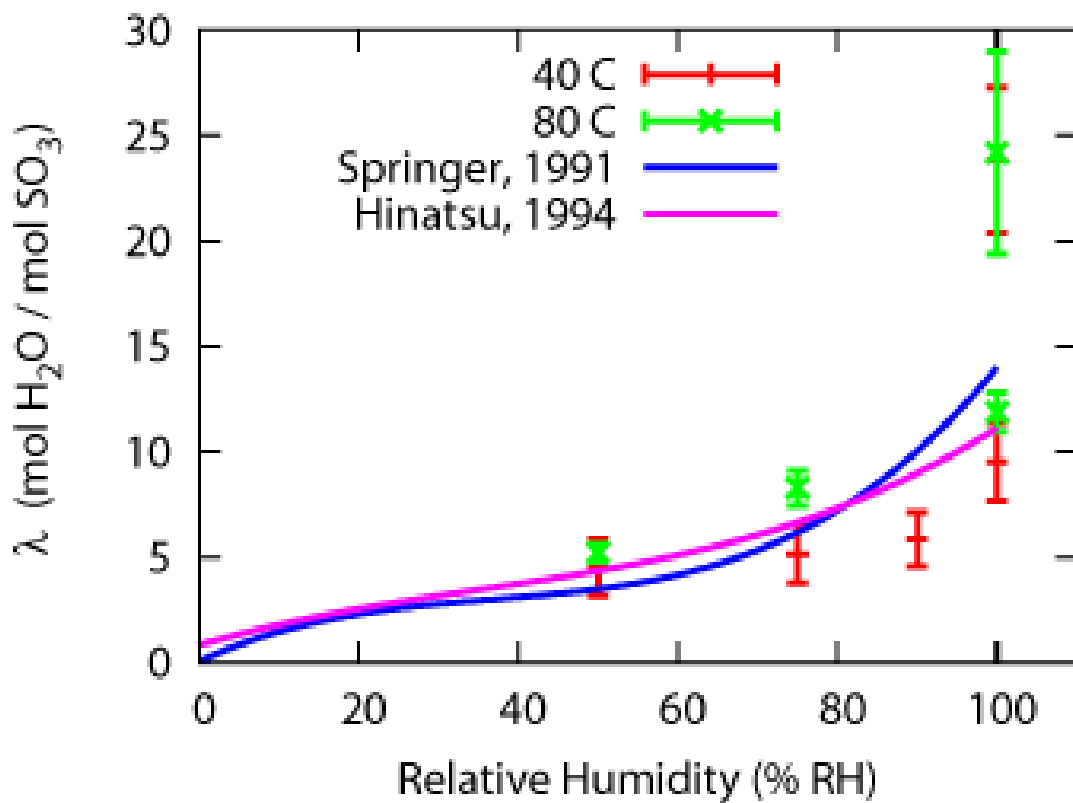


Figure 7: Water sorption as a function of inlet gas humidity. The uncertainty plotted is derived from counting statistics alone. The two solid lines are the correlation for λ as a function of activity derived from Springer, *et al*⁽²⁵⁾ and Hinatsu, *et al*⁽²⁶⁾.

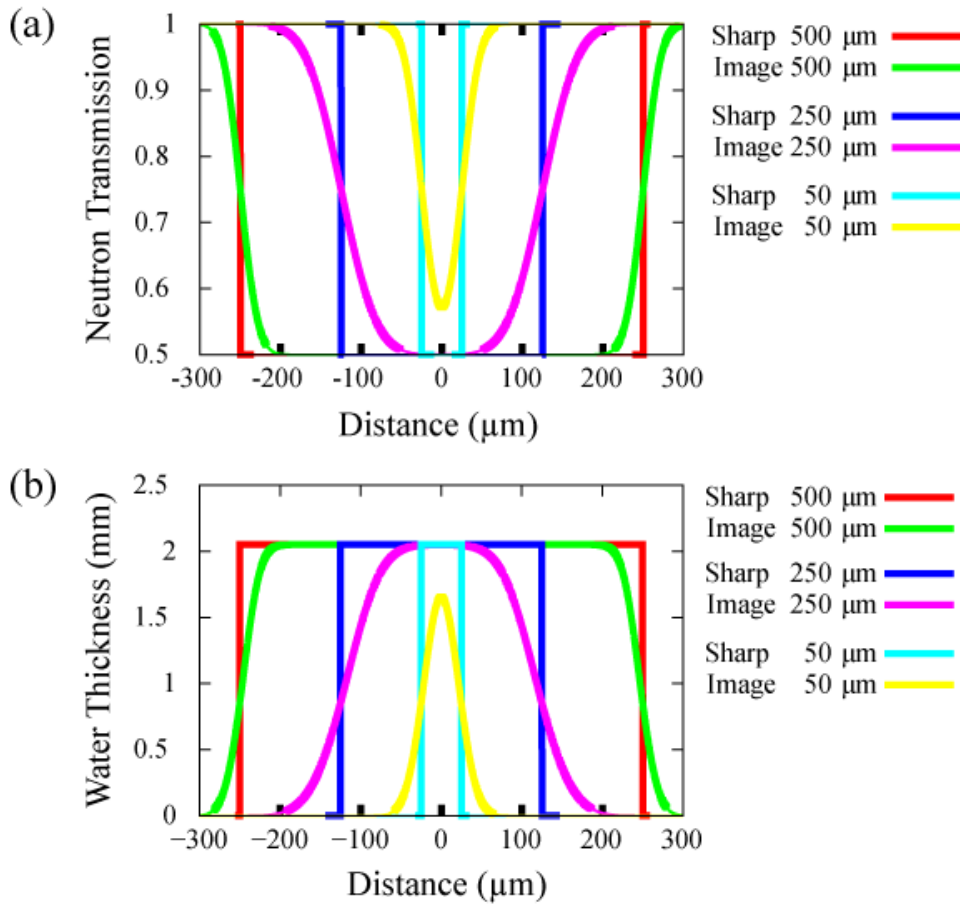


Figure 8: A two-dimensional, noiseless image was simulated of a slab of water that was 2 mm thick along the beam path ($t_w = 2$ mm) with a variable width transverse to the beam direction. The average transmission along the width of slab was from the simulated, blurry image is shown in (a), and is referred to as a the through-plane transmission profile. Taking the natural logarithm of the transmission profile yields the through-plane water profile shown (b).

Aperture #	Aperture Dimension	$\approx L/D$ (x,y)	Fluence Rate (cm⁻² s⁻¹)
5	15 mm	450	1.38E+07
4	10 mm	600	4.97E+06
3	3 mm	2000	5.23E+05
2	10 x 1 mm	600, 6000	6.54E+05
1	1 x 10 mm	6000, 600	7.17E+05

Table 1: The fluence rate and approximate L/D for the five apertures available at the NIST neutron imaging facility. The slits in position 1 and 2 reduce the geometric blur along one direction by about a factor of 5 over the previous configuration for use in high resolution imaging of the through-plane water content.

Spectrum Type	Mean Energy (meV)	μ_w (mm ⁻¹)	$\delta \mu_w$ (mm ⁻¹)
Thermal (BT-2)	25	0.338	0.001
Cold (NG-1)	3	0.645	0.002

Table 2: Attenuation coefficient measured in the calibration experiment. The uncertainty is the one-sigma fit error. The reduced-chi-square for each fit was of order 1.